Journal of Biomedical Optics

SPIEDigitalLibrary.org/jbo

Sensitivity analysis of near-infrared functional lymphatic imaging

Michael Weiler
Timothy Kassis
J. Brandon Dixon

SPIE

Sensitivity analysis of near-infrared functional lymphatic imaging

Michael Weiler, Timothy Kassis, and J. Brandon Dixon
Georgia Institute of Technology, George W. Woodruff School of Mechanical Engineering, Wallace H. Coulter Department of Biomedical Engineering, Parker H. Petit Institute for Bioengineering and Bioscience, IBB 2312, 315 Ferst Drive, Atlanta, Georgia 30332-0405

Abstract. Near-infrared imaging of lymphatic drainage of injected indocyanine green (ICG) has emerged as a new technology for clinical imaging of lymphatic architecture and quantification of vessel function, yet the imaging capabilities of this approach have yet to be quantitatively characterized. We seek to quantify its capabilities as a diagnostic tool for lymphatic disease. Imaging is performed in a tissue phantom for sensitivity analysis and in hairless rats for *in vivo* testing. To demonstrate the efficacy of this imaging approach to quantifying immediate functional changes in lymphatics, we investigate the effects of a topically applied nitric oxide (NO) donor glyceryl trinitrate ointment. Premixing ICG with albumin induces greater fluorescence intensity, with the ideal concentration being 150 μg/mL ICG and 60 g/L albumin. ICG fluorescence can be detected at a concentration of 150 μg/mL as deep as 6 mm with our system, but spatial resolution deteriorates below 3 mm, skewing measurements of vessel geometry. NO treatment slows lymphatic transport, which is reflected in increased transport time, reduced packet frequency, reduced packet velocity, and reduced effective contraction length. NIR imaging may be an alternative to invasive procedures measuring lymphatic function *in vivo* in real time. [DOI: 10.1117/1.JBO.17.6.066019]

Keywords: NIR imaging; near-infrared imaging; lymphatic imaging; ICG.

Paper 12060P received Jan. 30, 2012; revised manuscript received Apr. 6, 2012; accepted for publication Apr. 30, 2012; published online Jun. 8, 2012.

1 Introduction

The lymphatic system plays a critical role in regulating tissue fluid balance by draining the interstitial space and preserving protein concentrations to maintain oncotic pressure.[1] If the natural function of the lymphatic system is disrupted, several pathologies can develop, most notably lymphedema, which often results in irreversible tissue damage presumably through the disruption of lymphatic transport, thus leading to subsequent interstitial fluid stagnation and lipid accumulation in the affected tissues.[2] However, our current understanding of the lymphatic vasculature pales in comparison with the blood vasculature—a phenomenon that can be attributed partly to the lack of *in vivo* imaging techniques suitable for visualizing lymphatic vessels. In the case of lymphedema, in particular, a major limitation in the development of new treatments has been the lack of *in vivo* imaging diagnostics capable of quantifying differences in the dynamic pump function of lymphatic vessels in real time.[3]

Recently, the lymphatic system has garnered increased interest, as its roles in tumor metastasis,[4] dermal drug delivery,[5] chronic inflammation,[6] and lipid transport[7] are beginning to be appreciated. With the new understanding of the role of lymphatic vessels in disease processes and therapies, there is now a greater need for major advances in the diagnostic imaging tools available to adequately visualize and quantify lymphatic pump function. Since lymphatic flow is driven primarily through the contractility of collecting lymphatic vessels, [8,9] the ability to quantify lymphatic pump function through the imaging of functional lymphatic contractions and fluid flow would greatly improve the understanding of lymphatic contractile physiology and enhance the diagnosis of disease states. However, the two traditional gold standards of clinical lymphatic imaging, lymphoscintigraphy and magnetic resonance imaging (MRI), while very effective for systemic lymphatic mapping, are inadequate for the assessment of lymphatic function, because draining vessels are below the spatial resolution of MRI, and lymphoscintigraphy lacks the real-time temporal resolution needed to image the dynamics of lymphatic contractile function.[10–13]

Near-infrared (NIR) imaging technologies may provide the ideal solution to functional lymphatic imaging as both a research tool and a disease diagnostic, because NIR light resides in the optimal wavelength range, where light absorption and scattering are low in biological tissue and there is minimal autofluorescence. NIR imaging thus affords deeper penetration depths and excellent contrast and spatial resolution, all of which are vital for measuring lymphatic contractile properties.[14] NIR imaging with an FDA-approved fluorescent dye, indocyanine green (ICG), has recently emerged as a novel method for quantitative assessment of lymphatic function in animals and humans;[3,15–18] a technique in which ICG is injected intradermally, excited with a laser diode, and imaged with an NIR-sensitive detector as it is taken up by the lymphatic system.[19,20]

NIR lymphatic imaging, although in its infancy, has shown great promise to enhance the understanding of functional lymphatic transport characteristics both in health and disease, as the technology has the potential to develop into an early-stage diagnostic of lymphatic dysfunction.[19,21–23] Such a device would be strongly suited to enhance the diagnosis and treatment

Address all correspondence to: J. Brandon Dixon, Georgia Institute of Technology, George W. Woodruff School of Mechanical Engineering, Wallace H. Coulter Department of Biomedical Engineering, Parker H. Petit Institute for Bioengineering and Bioscience, IBB 2312, 315 Ferst Drive, Atlanta, GA 30332-0405. Tel: (404) 385-3915; Fax: (404) 385-1397; E-mail: dixon@gatech.edu.

0091-3286/2012/$25.00 © 2012 SPIE

of lymphatic disorders through the visualization and quantification of changes in functional lymphatic transport before clinical manifestations are present and tissue damage is irreversible. Current NIR lymphatic imaging technology has been quite successful at demonstrating differences in lymphatic function and architecture in patients who have already been diagnosed with lymphedema,[18,19,24] differences in lymphatic function in response to manual lymphatic drainage[25] and pneumatic pressure devices,[23] as well as a decline in lymphatic pumping pressure in response to aging.[26] However, it is currently unclear how effective this approach will be at predicting lymphedema disease risk or providing early detection, as most of its successes to date have involved showing differences in lymphatic function after significant deterioration has already occurred. Additionally, there has been very little experimentation or discussion on the effects of the interstitial environment on the various quantifiable parameters historically used with this technique, such as the effects of vessel depth and scattering on the ability to resolve differences in vessel diameter or the effects of protein binding on ICG fluorescence. Quantifying these and other effects will allow for potential optimization of component selection and configuration, will establish performance metrics of imaging functionality, and will provide more detail in regards to the limitations of the technique as a non-invasive tool for quantifying lymphatic function.

The purpose of this study, therefore, is to investigate these issues for characterizing and optimizing NIR imaging for the visualization and quantification of lymphatic pump function. Furthermore, the current state of the art for studying lymphatic contractile dynamics and their biophysical and molecular regulation *in vivo* requires invasive, terminal procedures,[27–30] but NIR lymphatic imaging may have the potential to generate similar data regarding lymphatic function in a completely noninvasive manner. Therefore, we will validate the performance of the NIR imaging system to detect functional changes in lymphatic transport by intentionally modulating lymphatic contractility *in vivo* using nitric oxide (NO) and performing *in vivo* NIR imaging to detect the resulting changes in lymphatic function. We expect NIR imaging to be able to detect functional changes in lymphatic transport after differential applications of NO, which may establish a novel research tool for studying the regulatory effects of NO on lymphatic pump function noninvasively *in vivo* in real time.

2 Materials and Methods

2.1 *Near-Infrared Functional Lymphatic Imaging System Setup*

The NIR lymphatic imaging device, which is depicted in Fig. 1, was developed using a 150 mW 808 nm laser diode (Thorlabs part no. M9-808-0150) powered by accompanying diode driver and temperature control boxes to provide excitation light. A 20 deg beam diffuser (Thorlabs part no. ED1-C20) was mounted in front of the diode to achieve a uniform excitation field of approximately 75 cm^2 with less than 1.9 mW/cm^2. Fluorescence emission centered at 840 nm was captured using a PIXIS 1024B back-illuminated CCD camera (Princeton Instruments) with an attached Infinity K2/SC video microscope lens (Edmund Optics) and a bandpass filter (CW: 840 nm, FWHM: 15 nm, Omega Optical). NIR images were recorded via a custom LabView (National Instruments) image acquisition code.

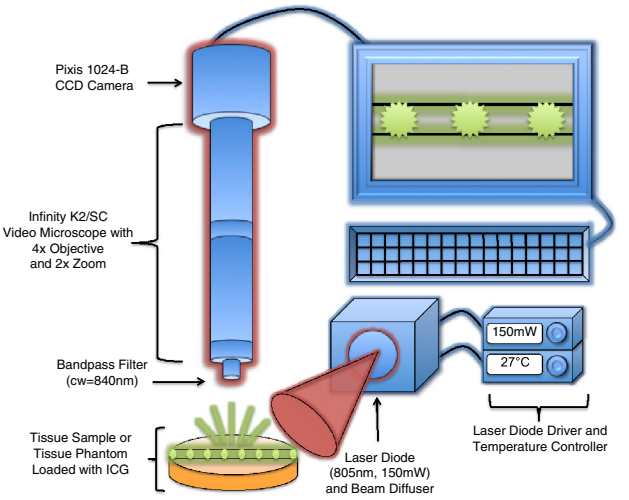

Fig. 1 NIR lymphatic imaging system schematic. Excitation light is provided by 150 mW 808 nm laser diode powered by accompanying diode driver and temperature control boxes. Emission light centered at 840 nm is captured by a CCD Camera with an Infinity K2/SC video microscope lens and a bandpass filter (CW: 840 nm, FWHM: 15 nm).

2.2 *ICG Solution Preparation*

To determine the optimal excitation and emission wavelength of ICG for use in NIR lymphatic imaging, we created an albumin-physiological salt solution (APSS) (in mM: 145.00 NaCl, 4.7 KCl, 2.0 $CaCl_2$, 1.17$MgSO_4$, 1.2NaH_2PO_4, 5.0 dextrose, 2.0 sodium pyruvate, 0.02 EDTA, 3.0 MOPS, and 10 g/L bovine serum albumin)[31] designed to mimic interstitial fluid, and we added a commonly used concentration of 250 μg/mL of ICG (Across Organics)[22] to simulate an injection of ICG into the interstitial space. For comparison purposes, the same concentration of ICG was also dissolved in 0.9% saline water. Peak excitation of both solutions was recorded using a spectrophotometer (Hitachi U-2900), and peak emission at the previously recorded peak excitation was recorded using a fluorometer (Shimazu RF-1501).

The optimal ICG solution for maximizing fluorescence yield within the dermal layer was determined by dissolving various concentrations of ICG ranging from 0.01 to 1,000 μg/mL in 0.9% saline and in APSS solutions with albumin concentrations ranging from 0 to 100 g/L. The various solutions were flowed through the tissue phantom at a depth of 2 mm to simulate flow through a dermal lymphatic vessel. The vessel was imaged using the NIR system, and fluorescence intensity was recorded for each sample to determine the optimal ICG and albumin concentrations. In order to quantify the enhancement of premixing ICG with albumin, follow-up testing was performed *in vivo* to compare the signal to noise ratio (SNR) of the optimal ICG/albumin solution (150 μg/mL ICG + 60 g/L albumin) and ICG alone (150 μg/mL ICG) both at the injection site and 10 cm downstream in the collecting vessel, where SNR was calculated as $\mathrm{SNR} = 20 \times \log(\frac{\mathrm{Fluorescence}}{\mathrm{Background}})$. Functional lymphatic testing (detailed below) was also performed to verify that premixing ICG with albumin does not alter lymphatic function, as measured by transport time, packet frequency, and packet velocity.

2.3 *Tissue Phantom Preparation*

In order to characterize the parameters of NIR lymphatic imaging in the dermis, a tissue phantom was created with the same

optical properties as the dermal layer. Mock lymphatic vessels of known diameters were created in the tissue phantom at known depths, thus affording complete control over the phantom and allowing idealized characterization of NIR imaging capabilities regarding spatial resolution and signal penetration depth. As can be seen in Fig. 2, the tissue phantom was molded in a standard petri dish using a mixture of 97.52% silicone elastomer base (Sylgard 184, Dow Corning), 2.22% Aluminum Oxide (Sigma Aldrich), and 0.26% cosmetic powder (Max Factor Crème Puff Deep Beige 42) according to previously published methods.[32] Channels were created in the tissue phantom molds by suspending standard copper electrical wire of known diameters at known depths in the mold prior to curing and removing the wires after curing. The tissue phantom was also connected to a syringe pump (PHD 2000, Harvard Apparatus) to flow various ICG solutions through the mock vessels for imaging, a schematic of which is depicted in Fig. 2(d).

2.4 *Sensitivity Analysis of NIR System*

Mock vessels of 1 mm diameter were created in a phantom at depths ranging from 1 to 10 mm in 1 mm increments, the optimal ICG solution (150 μg/mL ICG, 60 g/L albumin) was loaded into each of the mock vessels, and fluorescence intensity was recorded at each depth in order to characterize the change in signal sensitivity of the NIR system as a function of depth. Vessel diameter calculations were performed at all depths to characterize the scattering effect on apparent vessel diameter. Fluorescence intensity measurements were recorded for four conditions to quantify excitation light leakage: (1) CCD shutter closed (background), (2) excitation light source on without ICG in the phantom, (3) low concentration of ICG (1 μg/mL + 60 g/L albumin), and (4) ideal concentration of ICG (150 μg/mL + 60 g/L albumin).

ICG typically flows through lymphatic vessels in the form of discrete packets,[15,20] presumably due to valve closure that is known to occur during periods of short flow reversal, when a favorable pressure gradient exists to close the valve.[33,34] To mimic the pulsatile packet flow of ICG in lymphatic vessels, mock ICG packets were created by preloading a length of tubing with drops of ICG solution separated by olive oil (to prevent mixing of the ICG packets through diffusion). A syringe pump was then used to flow the packets of ICG through the tissue phantom at known velocities to test the accuracy of a custom lymph velocity quantification algorithm we developed. The algorithm, a similar version of which was first reported by Sharma et al. in 2007,[20] utilizes line intensity profiles placed sequentially along a lymphatic vessel in the direction of flow at known distances from each other [Fig. 3(a)]. The line intensity profiles record spikes when packets pass over that particular area [Fig. 3(b)], and by measuring the time between spikes in the three sequential line profiles, average velocity of packets can be calculated.

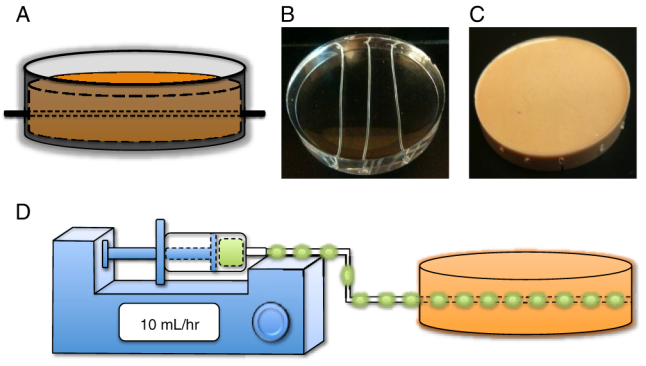

Fig. 2 Tissue phantom schematic and operation. (a) Tissue phantoms were molded in standard petri dishes using a mixture of 97.52% silicone elastomer base, 2.22% Aluminum Oxide, and 0.26% cosmetic powder. Channels were created in the tissue phantom molds by suspending standard electrical wire of known dimensions at known depths. (b) Image of the resulting channels after the molds are cured and the wires are removed. This is an example image created using 100% silicone to allow visualization of the channels. (c) Image of the final tissue phantom construct in which the channel outlets can be seen protruding from the side of the phantom. (d) The tissue phantom was connected to tubing containing preloaded "packets" of ICG to test the spatial and temporal resolution of the NIR imaging system. The flow rate through the tissue phantom was precisely controlled with a syringe pump, and the ICG packets were imaged as they passed through the phantom.

2.5 *In Vivo Imaging*

Lymphatic function was quantified *in vivo* in the tail of six-week-old female hairless rats (Charles River Laboratories, Wilmington, MA) that were divided into a treatment group and a control group ($n = 3$). The treatment group received a topical application of a glyceryl trinitrate ointment (GTNO) (0.2% wt/wt, Rectogesic, Care Pharmaceuticals, commercially available), which is an ointment with an NO donor group that has previously been reported to slow lymphatic transport time.[35]

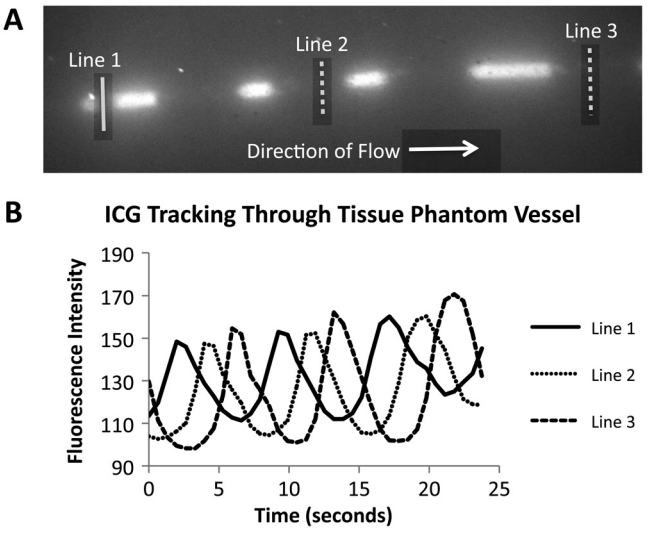

Fig. 3 Quantification of ICG packet travel through tissue phantom. Packets of ICG were created by separating small amounts of ICG with olive oil (to prevent mixing of separate packets) in a segment of tubing connected to the tissue phantom. A syringe pump was used to precisely control the flow rate of the fluid through the tubing/tissue phantom construct. A custom code was used to process the data by calculating intensity values over three line profiles placed sequentially along the channel. (a) Example image of ICG packets flowing through the tissue phantom at a depth of 1 mm. The three lines depicted show the placement of the three line integrals used in the processing algorithm to detect fluorescence intensity. (b) Example of the fluorescence intensity plots at the three line intensity profiles over time. Peaks in fluorescence intensity correspond to packets traveling over the lines. Fluid velocity can be calculated using the known dimensions of the channel and the time intervals between packets reaching sequential line profiles.

The control group did not receive any topical treatment. Both groups were anesthetized with an intramuscular injection of Fentanyl (0.12 mg/kg), Droperidol (6 mg/kg), and Diazepam (2.5 mg/kg given 10 minutes after Fentanyl/Droperidol). The treatment and control groups were then both given 10 μL intradermal injections of ICG (150 μg/mL ICG, 60 g/L albumin) in the tip of the tail (given one minute after the GTNO application for the treatment group).

The NIR lymphatic imaging system was positioned such that the excitation source and the field of view of the CCD emission detector were centered on the rats' tail 10 cm downstream (towards the base of the tail) from the injection site at the tip of the tail. The animals were imaged continuously from the time of injection until 20 min post-injection with a camera exposure time of 0.05 s. To evaluate lymphatic function in each of the rat subjects, three parameters were measured: the time necessary for the bolus injection of ICG to travel the 10 cm distance from injection site to emission recording site (transport time), the average velocity of the packets traveling through the field of view of the recording site, and the average frequency of packets passing through the field of view.

The transport time was calculated as the time between ICG injection and the arrival of fluorescence in the field of view 10 cm downstream from the injection site. The arrival of fluorescence was defined as a 20% increase in fluorescence intensity in the collecting vessel. An example of fluorescence arrival in the collecting vessel can be seen in Video 1, and a plot of fluorescence intensity over time during fluorescence arrival can be seen in Fig. 4.

Packet frequency and velocity were measured using plots of fluorescence intensity over time generated from two regions of interest (ROIs) in a collecting vessel. ROIs were placed approximately 3 to 6 mm apart in regions of the vessel exhibiting large fluctuations in fluorescence intensity over time, where packet movement could easily be visualized and quantified. Packet frequency and velocity measurements began 10 frames after the arrival of fluorescence (to allow fluorescence values to stabilize) and measured for a duration of 10 packets. Of the two vessels in the tail, measurements were taken only on the vessel first producing fluorescence. Average packet frequency was calculated as 10 packets divided by the time necessary for 10 packets to occur (in minutes). Average packet velocity was calculated as the distance between the two ROIs divided by the average time necessary for packets to travel between the two ROIs (as indicated by peaks in the intensity plots). Figure 5 shows control and GTNO treatment examples of ROI selection and intensity versus time plots of the 10 packets used for frequency and velocity measurement. Videos 2 and 3 show the 10 packet segment of ICG flowing through the collecting vessels associated with the intensity plots in Fig. 5 for normal and GTNO conditions, respectively.

To calculate the average delay time between contractions, we wrote a Matlab script that analyzes a given video sequence to find the region of highest fluctuation within the vessel. The fluorescence in this region was then quantified as a function of time, and that signal was processed by the code to calculate the average number of frames for each interval in which there was no fluorescence fluctuation. This value was multiplied by the time interval between frames and reported as the average delay time, t_d, for that vessel.

The data for each of the three functional imaging parameters were averaged for the treatment and control group, subsequently checked for normality using the Anderson-Darling test, and analyzed for statistical significance using a two-sample t-test.

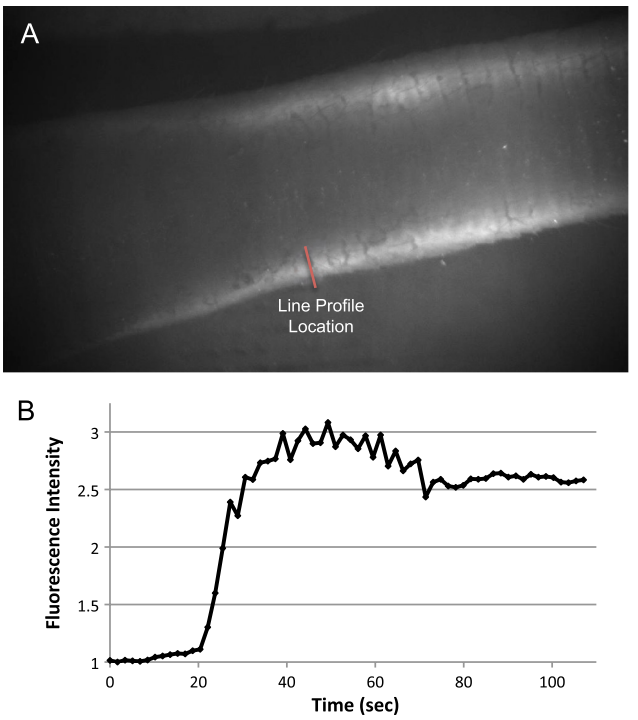

Fig. 4 Fluorescence intensity over time during fluorescence arrival. (a) Image showing location of line profile for fluorescence arrival example. (b) Example plot of intensity versus time during arrival of fluorescence. (Video 1) Example video of ICG fluorescence arrival in the collecting vessels of a normal rat 10 cm downstream from the intradermal injection. The timestamp represents time since injection. (Video 1, QuickTime, 4.2 MB). [URL: http://dx.doi.org/10.1117/1.JBO.17.6.066019.1].

2.5.1 *Quantifying Lymphatic Function Parameters*

We sought to define a term describing the average length a packet of fluid would travel between contraction events (referred to as the effective contraction length, L^*) as a metric of lymphatic function that could be calculated from parameters obtained with our system. Briefly, the time, t, it would take for the bolus injection to travel 10 cm along the tail is governed by the following equation:

$$t = \frac{1}{f}\frac{10\ \text{cm}}{L^*}$$

where f is the average frequency of contraction events. Knowing the rate of contraction events and the average time it takes for the moving front to reach a fixed distance allows us to estimate the average length each contraction event transports the fluid.

Each contraction event is composed of a delay time and a contraction time in which the vessel is actively moving the fluid along the contraction length L^*:

$$\frac{1}{f} = t_{L^*} + t_d$$

From this equation, we can estimate t_{L^*} given that we calculate the other two parameters from the image analysis. We also sought to develop a method for describing the systolic pumping

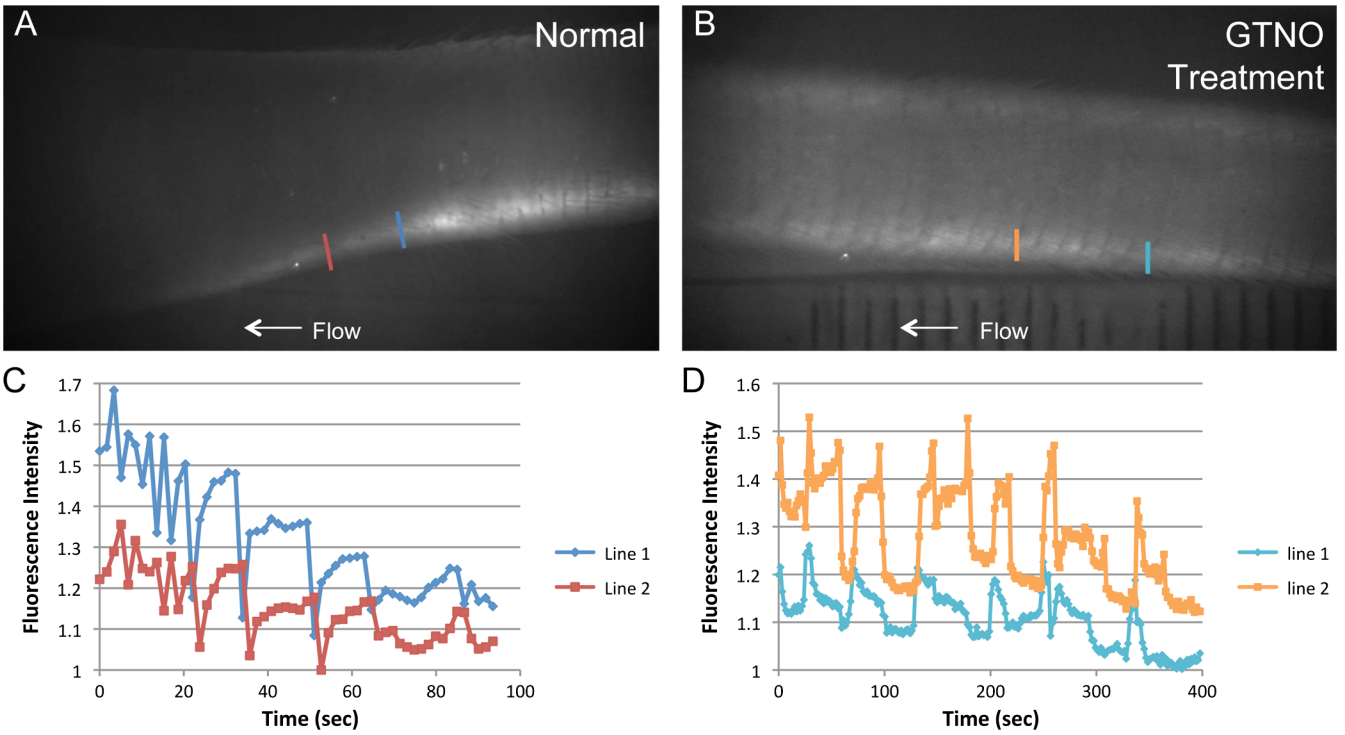

Fig. 5 Example intensity plots over time for normal and GTNO treatment conditions. (a) Image showing location of line profiles for normal condition example. (b) Image showing location of line profiles for GTNO treatment condition example. (c) Example plot of intensity versus time for normal condition. (d) Example plot of intensity versus time for GTNO treatment condition. (Video 2) An example video of ICG flowing through the two collecting vessels in the tail of a normal rat. The video lasts for the duration of 10 packets and is used to calculate packet frequency and velocity. The timestamp represents time after fluorescence arrival. (Video 3) An example video of ICG flowing through the two collecting vessels in the tail of a rat after GTNO treatment. The video lasts for the duration of 10 packets and is used to calculate packet frequency and velocity. The timestamp represents time after fluorescence arrival (Video 2, QuickTime, 3.1 MB); [URL: http://dx.doi.org/10.1117/1.JBO.17.6.066019.2] (Video 3, QuickTime, 12.6 MB) [URL: http://dx.doi.org/10.1117/1.JBO.17.6.066019.3].

power of the vessel from parameters measured by our system. During a contraction event, the fluid packet accelerates to a maximum velocity and then decelerates back to rest, having traveled a distance L^* over the entire cycle. If we assume that these two events are split evenly over this cycle, then the distance traveled by the packet during the systolic phase is $L^*/2$. To estimate the acceleration of the fluid packet during the systolic phase, we divide the average maximum packet velocity (which is measured as described above), V_p, by the duration of systole, which we estimate as $t_{L^*}/2$. From these approximations, the systolic pumping power can be estimated as

$$P_s = \left[m \frac{V_p}{t_{L^*}/2} \frac{L^*}{2} \right] \frac{1}{t_{L^*}/2},$$

where m is the mass of the fluid packet. While we do not know m, we can report the parameter

$$\left[\frac{V_p}{t_{L^*}} L^* \right] \frac{1}{t_{L^*}/2}$$

as the average systolic pumping power per unit mass.

3 Results

3.1 *ICG Spectrum and Fluorescence*

The excitation peaks for ICG dissolved in saline and APSS were approximately 785 and 805 nm, respectively, while the emission peaks of ICG in saline and APSS were approximately 815 and 840 nm, respectively (Fig. 6).

ICG fluorescence is highly dependent on albumin concentration, and the intensity reached a maximum at an albumin concentration of 60 g/L (902.8 μM) [Fig. 7(a)], and the maximum fluorescence yield at this albumin concentration was produced at

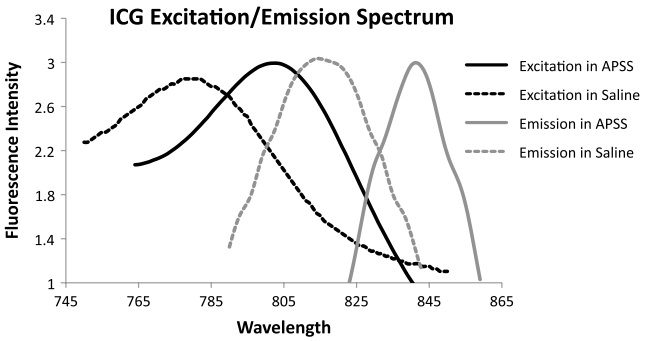

Fig. 6 ICG dissolved in albumin salt solution (APSS) exhibits a shift in the excitation/emission spectrum. Excitation and emission curves were generated for ICG (250 μg/mL) dissolved in 0.9% saline (dotted lines) and APSS (solid lines). A shift of approximately 20 nm was observed in the excitation spectrum of ICG dissolved in APSS versus saline, with peak fluorescence occurring at 805 and 785 nm, respectively. A shift of approximately 25 nm was observed in the emission spectrum of ICG dissolved in APSS versus saline, with peak fluorescence occurring at 840 and 815 nm, respectively. These spectra guided the design of excitation and emission detection wavelengths of the NIR imaging system.

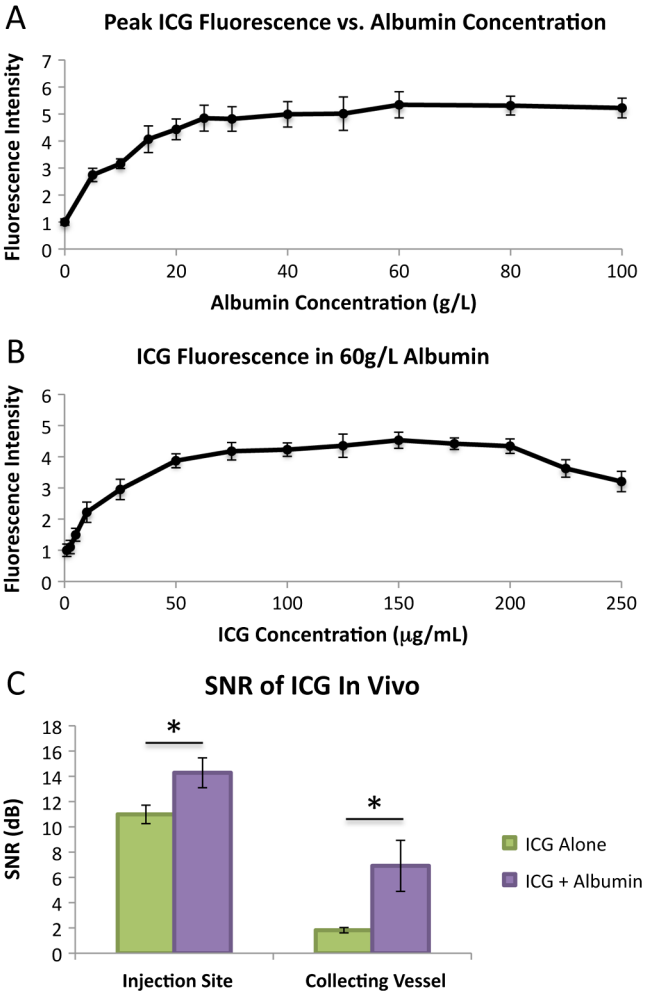

Fig. 7 Prebinding ICG with albumin enhances fluorescence and the resulting SNR upon *in vivo* intradermal injection. Fluorescence intensity through the phantom at a depth of 2 mm was measured for various concentrations of ICG and albumin to optimize the two concentrations to produce maximum fluorescence intensity of the ICG solution. (a) Peak ICG fluorescence intensity was measured as a function of albumin concentration in APSS ranging from 0 g/L albumin to 100 g/L albumin. Peak ICG fluorescence was produced at 60 g/L albumin. (b) Fluorescence intensity of ICG dissolved in 60 g/L was measured as a function of ICG concentration to determine the final concentrations of the optimal ICG solution for producing maximum fluorescence intensity. Maximum fluorescence intensity was measured at an ICG concentration of 150 μg/mL. (c) 150 μg/mL ICG solution and 150 μg/mL ICG premixed with 60 g/L albumin were injected into rat tails, and the signal to noise ratio (SNR) was calculated for each sample at the injection site and 10 cm downstream in the collecting lymphatic vessel. ICG premixed with albumin produced more than a four-fold increase in SNR compared to ICG alone from 1.8 to 7.8 dB in the collecting vessels and an increase from 10.9 to 14.2 dB at the injection site. Error bars represent standard deviation. $* = p < 0.05$.

an ICG concentration of 150 μg/mL (193.5 μM) [Fig. 7(b)]. Thus the solution producing maximal fluorescence was 150 μg/mL ICG and 60 g/L albumin. When injected into a rat tail, premixing 150 μg/mL ICG with 60 g/L albumin produced a greater SNR as compared to 150 μg/mL ICG alone with more than a four-fold increase in SNR observed in the collecting vessels [Fig. 7(c)] ($p < 0.05$). Additional functional lymphatic testing was performed in response to ICG and ICG/albumin injections, and no significant differences were observed in transport time, packet frequency, or packet velocity (Fig. 8).

3.2 *Tissue Phantom Sensitivity Analysis*

The minimum detectable concentration of ICG at 2 mm depth was 0.1 μg/mL, and ICG emission was detectable as deep as 6 mm with the signal at depths below 7 mm being indistinguishable from background (Fig. 9). Quantifying excitation light leakage showed a four-fold increase of signal over the thermal noise background. However, even low ICG concentrations produced a signal much larger than that due to leakage, and values of fluorescence typically seen in the vessel *in vivo* have fluorescence intensity values 14-fold greater than the excitation light source (Fig. 10). Vessel diameter calculations were very accurate at a depth of 1 mm with a 0.74% error, but error increased with depth to over 1,000% at 5 mm and was incalculable beyond 5 mm due to excessive scattering. The results also show that the calculated velocities were within 1% of the true velocities over a range from 0.15 to 1.5 mm/s (Fig. 11).

3.3 *Quantifying Functional Effects of NO on Lymphatics In Vivo*

Application of GTNO significantly reduced lymphatic function (Fig. 12). Video 2 shows normal lymph propulsion through the tail of a control rat, while Video 3 shows significantly reduced

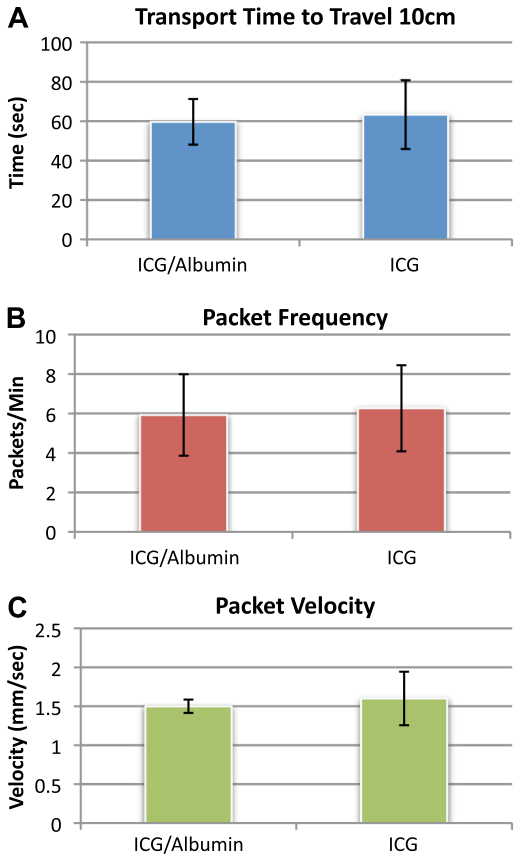

Fig. 8 Premixing ICG with albumin does not alter lymphatic function compared to ICG alone. Results of functional lymphatic testing reveal no significant differences between injection of ICG alone and ICG plus albumin in the tails of rats ($n = 3$). (a) No significant difference in transport time to travel 10 cm. (b) No significant difference in packet frequency. (c) No significant difference in packet velocity.

lymphatic pump function in a rat after GTNO application. Transport time increased from 60 s under normal conditions to 414 s after GTNO application ($p < 0.01$). Packet frequency decreased from 5.92 packets per minute and under normal conditions to 3.1 packets per minute after GTNO application ($p < 0.05$). Packet velocity decreased from 1.5 mm/s under normal conditions to 0.48 mm/s after GTNO application ($p < 0.05$). GTNO application decreased effective contraction length from 17.6 to 5.1 mm ($p < 0.0005$). Contraction duration after GTNO application was significantly increased from 4.1 to 5.4 s ($p < 0.05$), and systolic pumping power per unit mass was drastically reduced after GTNO application from 1.25 to 0.024 mm^2/s^3.

4 Discussion and Conclusions

4.1 *Effects of Protein Binding on ICG Fluorescence*

The NIR lymphatic imaging system that we developed in this study represents a departure from the setup of many of the NIR lymphatic imaging systems previously reported in that we premixed ICG with albumin, and our system used an excitation wavelength of 808 nm and emission wavelength centered at 840 nm.[18,21] Previous systems have used excitation sources of 785 nm, presumably because of the large availability of diodes at this wavelength. Our results indicate that ICG produces more than a three-fold increase in fluorescence when it binds to albumin, and the peak excitation and emission wavelengths are 805 and 840 nm, respectively. The same effect is observed when ICG is introduced in APSS, thus suggesting that ICG binds to albumin in the interstitial space. Therefore, ICG-based NIR lymphatic imaging systems that excite at 808 nm and capture emission centered at 840 nm will achieve higher SNR.

ICG has previously been shown to rapidly and completely bind to albumin in plasma.[36] Given that albumin concentration in the interstitium is approximately half of its concentration in plasma,[37] and the albumin concentration in lymph has been measured to be about 40% of its value in plasma,[38] it is reasonable to assume that all of the ICG present in lymph is bound to albumin as well. This assumption is further justified by the fact that the molecular weight of ICG (775 daltons) does not preclude it to lymphatic partitioning. Thus, the preferential uptake of ICG into lymphatics that is observed following dermal injections suggests that it must be bound to something of a large enough size to require lymphatic transport. Since albumin is the most prevalent soluble protein in the interstitium, is preferentially taken up into lymphatics after a dermal injection, and binds readily to ICG, it follows that even after dermal injection of ICG alone, the dye in the lymph is bound to albumin. Premixing ICG with albumin prior to injection thus not only increases the fluorescence of the dye, but it also eliminates interstitial albumin availability as a limiting factor in ICG uptake into lymphatics.

This approach to ICG delivery could be of particular importance when using this imaging technique in pathologies such as lymphedema, as the disease often results in accumulation of macromolecular proteins in the interstitium[39] that could significantly influence the uptake of injected ICG, confounding the interpretation of the experimental data. It is important to note that the injection of 10 μl of 60 mg/ml albumin solution, while a very small volume, will disrupt the local gradients governing plasma filtration, temporarily increasing fluid extravasation from the blood and thus lymph formation. However, these values are well within the range of what the lymphatics would be expected to resolve during a mild inflammatory event, as average flow rates in a collecting lymphatic of fasted rats have been reported to range from 40 nl/ min to 200 μl/ min depending on the vessel size and state of hydration.[33,40]

It should be noted that Ashitate et al. recently reported that ICG alone was a better fluorophore for lymphatic visualization in the thoracic duct than ICG prebound to albumin,[41] but there are several differences in experimental setup and technique worth exploring. Firstly, the NIR imaging system they employ excites at 760 nm, while our system is optimized to excite ICG bound to albumin, which is maximally excited at 805 nm. Their experimental setup also does not require imaging through the dermis and thus does not have to account for scattering and absorption effects, since most scattering and absorption occurs in the dermis. Interestingly, Ashitate and colleagues report a SNR for ICG of about 2, which is very similar to our results for ICG in collecting vessels. Given that we also report a SNR of nearly 8 for ICG bound to albumin in collecting vessels, we are confident prebinding ICG to albumin provides a more fluorescent tracer. Translating this technique into the clinic will produce additional regulatory challenges, but premixing the dye with autologous serum prior to dermal injection could provide one route of protein-bound ICG delivery.

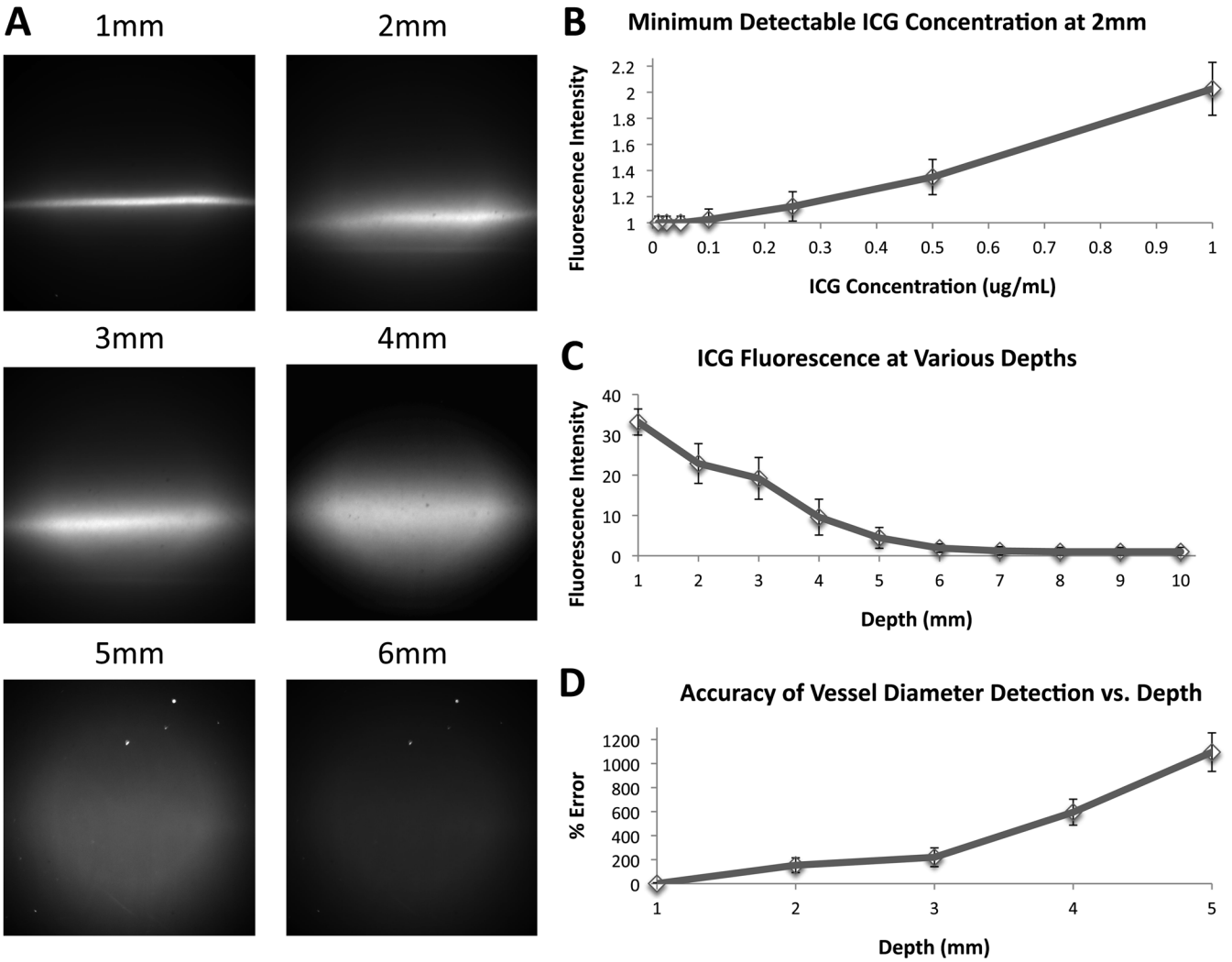

Fig. 9 ICG can be detected up to a depth of 6 mm with minimal loss of spatial resolution at a depth of up to 3 mm. The optimal concentration of ICG solution (150 μg/mL ICG, 60 g/L albumin) was flowed through the tissue phantom at depths between 1 and 10 mm in 1 mm increments to determine how signal sensitivity changes with depth. (a) Example images of ICG flowing through the tissue phantom from 1 to 6 mm, which was the depth limit of detection. (b) Plot of minimum detectable ICG concentration at 2 mm depth in the tissue phantom. Minimum detectable ICG concentration was 0.1 μg/mL. (c) Plot of ICG fluorescence intensity as a function of depth showing fluorescence intensity decreased successively with depth until 7 mm, which was indistinguishable from background. The depth limit of signal detection was 6 mm. (d) The apparent diameter of the channels at each depth was measured and compared to the true diameter of the channel to determine the accuracy of vessel diameter detection as a function of depth. At 1 mm, there was a 0.74% error between the true diameter and the measured diameter. Percent error increased with depth to a maximum of 1,095.06% error at 5 mm.

4.2 *Tissue Phantom Sensitivity Analysis*

The tissue phantom was constructed to recapitulate characteristics of lymphatic vessels *in vivo* that are essential to parameters historically quantified in NIR imaging, such as vessel morphology and propulsion frequency and velocity. Specifically, we constructed channels of similar size to lymphatics and imbedded them in a phantom with effective absorption and scattering coefficients of skin at depths characteristic of dermal lymphatics *in vivo*. According to our tissue phantom sensitivity analysis, the NIR lymphatic imaging system was capable of detecting ICG fluorescence as deep as 6 mm. However, scattering effects resulted in a deterioration of spatial resolution with increasing depth, and geometric vessel features became difficult to accurately identify below a depth of 3 mm. These results suggest that the NIR lymphatic imaging system is best used to detect vessel geometry and architecture above a 3 mm depth, but an assessment of gross ICG accumulation and transport *in vivo* can be obtained as deep as 6 mm (or perhaps deeper if features being resolved are greater than 1 mm, such as lymph nodes). Given that the average human skin layer is between 1 and 3 mm thick,[42] these imaging characteristics are well suited for imaging dermal lymphatic function. Clinically, however, lymphatic diseases often result in a severe remodeling of the dermis, and fibrosis and lipid deposition can increase the thickness of the dermis well beyond this 3 mm limit.[39]

In addition to chronic lymphedema resulting in a thickening of the dermis, it is likely that the optical properties of the tissue itself would change as the angiogenesis, adipogenesis, and fibrosis often associated with lymphedema would change the absorption and scattering coefficients of the dermal layer. Therefore, care should be taken in interpreting clinical data from ICG injections in patients with lymphatic disease, as the appearance of hyperplastic or dilated lymphatics could be due in part to

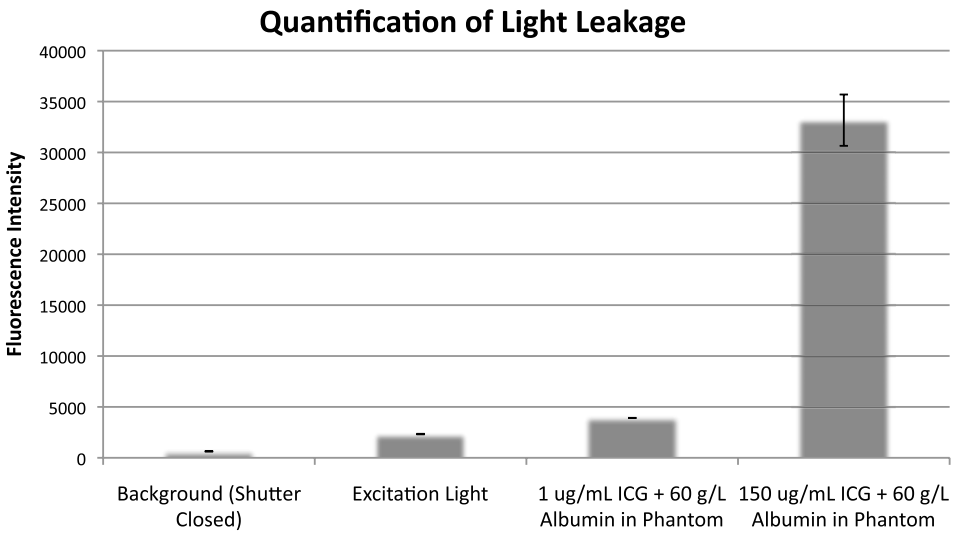

Fig. 10 Characterization of excitation light leakage. Intensity values were quantified for four conditions: (1) CCD shutter closed (background), (2) excitation light source on and phantom present without ICG, (3) low concentration of ICG in tissue phantom (1 μg/mL + 60 g/L albumin), and (4) ideal concentration of ICG (150 μg/mL + 60 g/L albumin). The results show that the excitation light produces a four-fold increase in intensity over background, but the ideal concentration of ICG produces a 14-fold increase in intensity over the excitation light source, which corresponds to a SNR of 23.1.

changes in the thickness and the optical properties of the diseased limb, thus increasing the apparent diameter of vessels in these patients. Future studies are warranted to determine how exactly these changes would affect the ability of NIR imaging to assess lymphatic function in diseased patients.

The primary tool in functional ICG imaging is the ability to quantify the kinetics of packet flow in lymphatic vessels *in vivo* that presumably occur due to the fluctuating pressure gradients in coordination with lymphatic valves creating segmented flow of the dye. While our phantom does not contain these valves or the intrinsic mechanics that promote lymph transport, we have artificially reproduced this packet flow at a physiologically relevant depth in the phantom to quantify our system's accuracy for measuring packet velocity in the presence of a scattering dermal layer, and we have demonstrated excellent accuracy in measuring velocity. Most NIR lymphatic imaging is performed giving an intradermal ICG injection and monitoring transport through dermal collecting vessels, which we have validated can be achieved with our device with a high degree of accuracy. Future work to enhance the device should focus on the implementation of diffusion theory (e.g., using a Monte Carlo approach to predict light propagation through a tissue of known optical properties) to predict scattering effects and recreate a more accurate image of vessel geometry at various depths.[43]

4.3 *Quantifying Functional Effects of NO on Lymphatics In Vivo*

In this study, we showed for the first time that immediate changes in lymphatic function resulting from the introduction of NO can be detected using non-invasive NIR lymphatic imaging. Our findings, that GTNO significantly reduces lymphatic transport, corroborates existing knowledge that NO has an inhibitory effect on lymphatic pump function.[29,31,35] We have shown that NIR lymphatic imaging can provide real-time *in vivo* measurements of lymphatic pump function in response to NO, which has never previously been available, and may help to further elucidate the relationship between NO and lymphatic contractile regulatory mechanisms. The ability to measure this response non-invasively would be particularly useful given recent findings that certain immune cells migrate to the lymphatics and release NO as a means of regulating local lymphatic draining.[29]

The gold standard for quantifying lymphatic pump function has been to utilize diameter tracking of contracting vessels to calculate parameters such as stroke volume and ejection fraction. These temporal traces of diameter changes have been achieved in isolated vessel preparations,[31,44] invasive *in vivo* intravital brightfield microscopy,[33,45] and more recently through invasive intravital fluorescence microscopy using vessels filled with FITC labeled dextran.[29] All of these approaches require invasive surgery to access and visualize the lymphatics, thus allowing for accurate diameter tracings. While the approach reported here has the advantage of being non-invasive, the scattering effects of the dermal layer and the lower frame rates do not currently provide the necessary spatial and temporal resolution to achieve accurate diameter tracings, which explains why this and other NIR lymphatic imaging systems have been unable to quantify these more traditional metrics of pump function. Thus we sought to define quantitative metrics of pump function

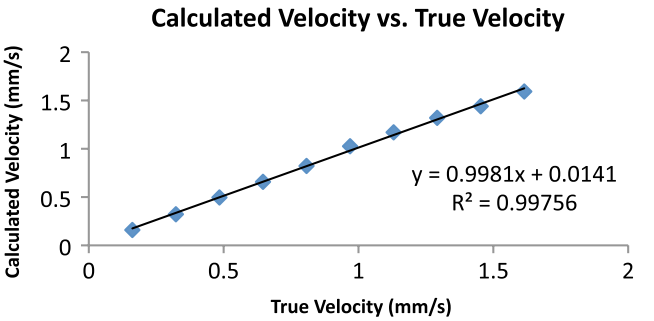

Fig. 11 Calculated packet velocity predicts true velocity with less than 1% error. Packets were flowed through the tissue phantom at a depth of 3 mm at velocities ranging from 0.15 to 1.5 mm/s. Velocities were calculated using a custom algorithm and compared to the known true velocities. Calculated velocities were accurate to within less than 1% error.

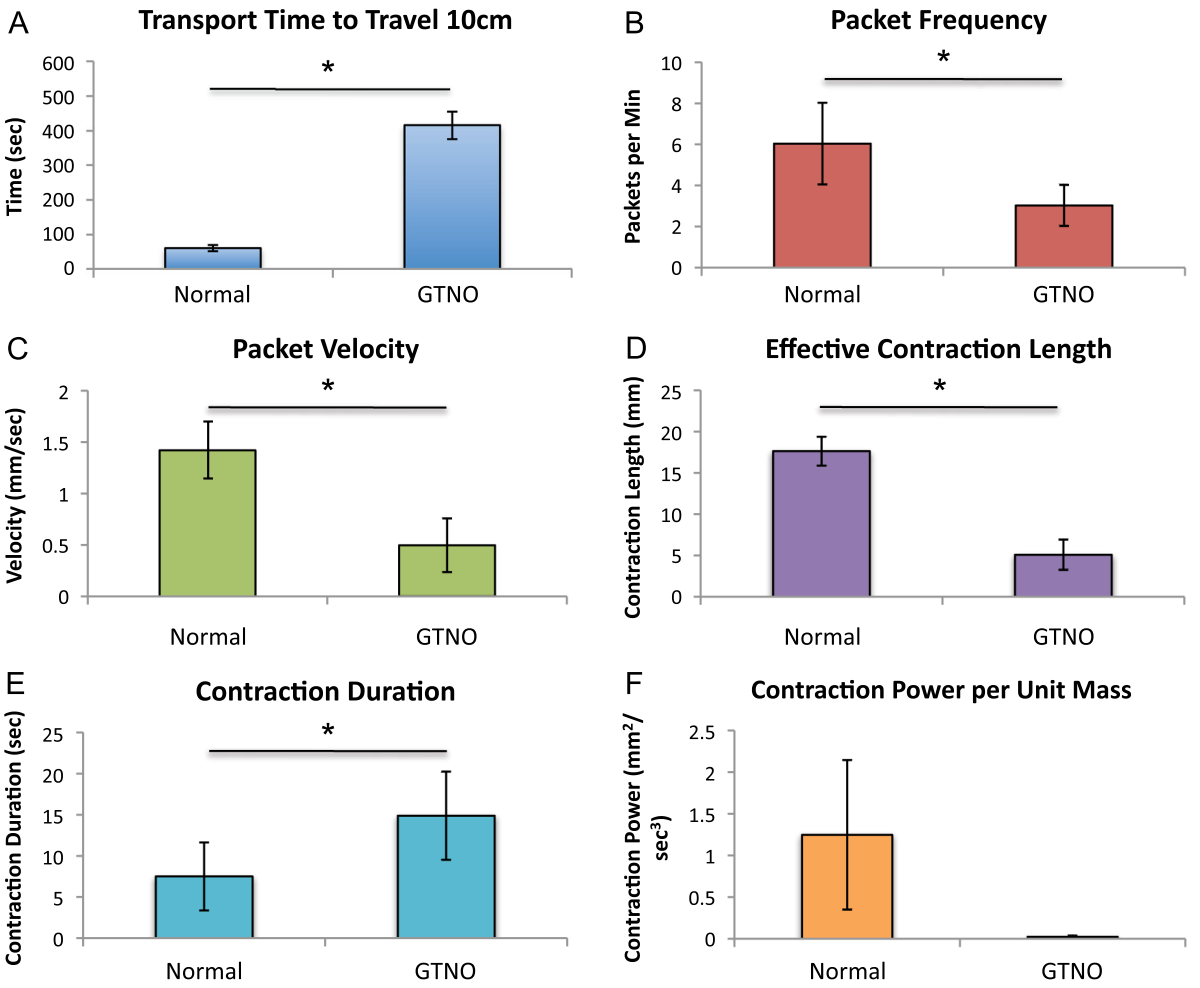

Fig. 12 Dermal nitric oxide delivery significantly reduces lymphatic pump function. 10 μL of ICG (150 μg/mL ICG, 60 g/L albumin) was injected intradermally into the tip of the tail of hairless rats divided into a treatment group that received a topical application of glyceryl trinitrate ointment (GTNO) prior to ICG injection ($n = 4$) and a control group that did not receive any treatment prior to ICG injection ($n = 4$). The NIR lymphatic imaging system was positioned to view the tail 10 cm downstream (towards the base of the tail) from the injection site. (a) The time required for the initial bolus injection of ICG to travel 10 cm downstream (transport time) significantly increased after GTNO application. (b) Packet frequency was significantly reduced after GTNO application. (c) Packet velocity was significantly reduced after GTNO application. (d) Effective contraction length was significantly decreased after GTNO application. (e) Contraction duration was significantly increased after GTNO application. (f) Contraction power per unit mass was decreased after GTNO treatment. $* = p < 0.005$.

similar to these parameters that could be calculated from our system, namely effective contraction length and systolic pumping power.

Effective contraction length describes, on average, how far a packet of fluid would travel down the lymphatic vessels before another contraction event is needed. Stronger contractions would propel fluid further (assuming that the immediate downstream valves are open), when compared to weaker contractions with lower ejection fractions. Systolic pumping power provides an estimation of the average power generated per unit mass by lymphatic pumping. A calculation of the actual power would require knowing the mass of the fluid packet, but this is difficult to estimate, since accurate diameter measurements are difficult to achieve given the limitations of NIR imaging discussed above. It is likely that this mass would be different between treatment groups, since it is known that NO increases the vessel diameter.[31] However, any changes that would occur in packet mass due to vessel dilation would be small (~2-fold increase) when compared to the changes seen in the power per unit mass parameter (~50-fold decrease). Both of the new parameters developed here demonstrate the potential to describe remarkable differences in lymphatic pump function that could be difficult to capture when tracking packet frequency or velocity alone.

Our findings also have the potential to establish NIR lymphatic imaging as an early-stage lymphatic disease diagnostic. To date, NIR imaging has been reported in the literature to be capable of identifying differences in lymphatic pump function between healthy states and several late-stage disease states.[19,22,24] However, given that most lymphatic disorders are characterized by a progressive deterioration of lymphatic pump function prior to the presentation of clinical manifestations, NIR imaging may be capable of detecting changes in lymphatic pump function in the very early stages of the disease before visible symptoms begin to present. Our findings suggest that NIR imaging is very sensitive to detecting differences in lymphatic transport function and could be used as a screening mechanism for patients at a high risk for developing lymphatic disorders, such as post-mastectomy breast cancer patients. In this way, corrective measures could be taken before irreversible

tissue damage would occur, thus improving patient outcomes with lymphatic diseases.

Acknowledgments

This work was funded by NIH Grant NHLBI R00HL091133, the Georgia Tech Research Foundation, a graduate fellowship from the U.S. Department of Education's Graduate Assistance in Areas of National Need (GAANN) program, and a graduate fellowship from NIH NIGMS Training Grant on Cell and Tissue Engineering (T32 GM008433).

References

1. R. M. Dongaonkar et al., "Balance point characterization of interstitial fluid volume regulation," *Am. J. Physiol. Regul. Integr. Comp. Physiol.* **297**(1), R6–R16 (2009).
2. K. Radhakrishnan and S. G. Rockson, "The clinical spectrum of lymphatic disease," *Ann. N. Y. Acad. Sci.* **1131**(1), 155–184 (2008).
3. J. C. Rasmussen et al., "Lymphatic imaging in humans with near-infrared fluorescence," *Curr. Opin. Biotechnol.* **20**(1), 74–82 (2009).
4. T. Karpanen and K. Alitalo, "Molecular biology and pathology of lymphangiogenesis.," *Annu. Rev. Pathol.* **3**(1), 367–397 (2008).
5. A. J. Harvey et al., "Microneedle-based intradermal delivery enables rapid lymphatic uptake and distribution of protein drugs," *Pharm. Res.* **28**(1), 107–116 (2011).
6. G. Jurisic and M. Detmar, "Lymphatic endothelium in health and disease.," *Cell Tissue Res.* **335**(1), 97–108 (2009).
7. J. B. Dixon, "Lymphatic lipid transport: sewer or subway?," *Trends Endocrinol. Metabol.* **21**(8), 480–487 (2010).
8. M. Muthuchamy et al., "Molecular and functional analyses of the contractile apparatus in lymphatic muscle," *FASEB J.* **17**(3), 920–922 (2003).
9. P.-Y. von der Weid and D. C. Zawieja, "Lymphatic smooth muscle: the motor unit of lymph drainage," *Int. J. Biochem. Cell Biol.* **36**(7), 1147–1153 (2004).
10. T. Barrett, P. L. Choyke, and H. Kobayashi, "Imaging of the lymphatic system: new horizons," *Contrast Media Mol Imag.* **1**(6), 230–245 (2006).
11. B. Misselwitz, "MR contrast agents in lymph node imaging," *Eur. J. Radiol.* **58**(3), 375–382 (2006).
12. S. T. Proulx et al., "Quantitative imaging of lymphatic function with liposomal indocyanine green," *Cancer Res.* **70**(18), 7053–7062 (2010).
13. R. Sharma et al., "New horizons for imaging lymphatic function," *Ann. N. Y. Acad. Sci.* **1131**(1), 13–36 (2008).
14. J. Rao, A. Dragulescu-Andrasi, and H. Yao, "Fluorescence imaging in vivo: recent advances," *Curr. Opin. Biotechnol.* **18**(1), 17–25 (2007).
15. S. Kwon and E. M. Sevick-Muraca, "Noninvasive quantitative imaging of lymph function in mice," *Lymphat. Res. Biol.* **5**(4), 219–232 (2007).
16. S. Kwon, "Functional lymphatic imaging in tumor-bearing mice," *J. Immunol. Methods* **360**(1), 167–172 (2010).
17. N. Unno et al., "Quantitative lymph imaging for assessment of lymph function using indocyanine green fluorescence lymphography," *Eur. J. Vasc. Endovasc. Surg.* **36**(2), 230–236 (2008).
18. J. C. Rasmussen et al., "Human lymphatic architecture and dynamic transport imaged using near-infrared fluorescence," *Transl. Oncol.* **3**(6), 362–372 (2010).
19. N. Unno et al., "Preliminary experience with a novel fluorescence lymphography using indocyanine green in patients with secondary lymphedema," *J. Vasc. Surg.* **45**(5), 1016–1021 (2007).
20. R. Sharma et al., "Quantitative imaging of lymph function," *Am. J. Physiol.-Heart C* **292**(6), H3109 (2007).
21. N. Unno et al., "A novel method of measuring human lymphatic pumping using indocyanine green fluorescence lymphography," *J. Vasc. Surg.* **52**(4), 946–952 (2010).
22. E. Sevick-Muraca et al., "Imaging of lymph flow in breast cancer patients after microdose administration of a near-infrared fluorophore: feasibility study1," *Radiology* **246**(3), 734–741 (2008).
23. K. Adams et al., "Direct evidence of lymphatic function improvement after advanced pneumatic compression device treatment of lymphedema," *Biomed. Opt. Express* **1**(1), 114–125 (2010).
24. E. A. Maus et al., "Near-infrared fluorescence imaging of lymphatics in head and neck lymphedema," *Head Neck* **34**(3), 448–453 (2010).
25. I.-C. Tan et al., "Assessment of lymphatic contractile function after manual lymphatic drainage using near-infrared fluorescence imaging," *Arch. Phys. Med. Rehabil.* **92**(5), 756–764 (2011).
26. N. Unno et al., "Influence of age and gender on human lymphatic pumping pressure in the leg," *Lymphology* **44**(3), 113–120 (2011).
27. J. B. Dixon et al., "Measuring microlymphatic flow using fast video microscopy," *J. Biomed. Opt.* **10**(6), 064016 (2005).
28. J. B. Dixon et al., "Image correlation algorithm for measuring lymphocyte velocity and diameter changes in contracting microlymphatics," *Ann. Biomed. Eng.* **35**(3), 387–396 (2007).
29. S. Liao et al., "Impaired lymphatic contraction associated with immunosuppression," *Proc. Natl. Acad. Sci. USA* **108**(46), 18784–18789 (2011).
30. H. G. Bohlen, O. Y. Gasheva, and D. C. Zawieja, "Nitric oxide formation by lymphatic bulb and valves is a major regulatory component of lymphatic pumping," *Am. J. Physiol.-Heart C* **301**(5), H1897–H1906 (2011).
31. A. A. Gashev, M. J. Davis, and D. C. Zawieja, "Inhibition of the active lymph pump by flow in rat mesenteric lymphatics and thoracic duct," *J. Physiol.* **540**(3), 1023–1037 (2002).
32. M. Lualdi et al., "A phantom with tissue-like optical properties in the visible and near infrared for use in photomedicine," *Laser. Surg. Med.* **28**(3), 237–243 (2001).
33. J. B. Dixon et al., "Lymph flow, shear stress, and lymphocyte velocity in rat mesenteric prenodal lymphatics," *Microcirculation* **13**(7), 597–610 (2006).
34. M. J. Davis et al., "Determinants of valve gating in collecting lymphatic vessels from rat mesentery," *Am. J. Physiol.-Heart C* **301**(1), H48–H60 (2011).
35. M. Saul et al., "A pharmacological approach to first aid treatment for snakebite," *Nat. Med.* **17**(7), 809–811 (2011).
36. G. R. Cherrick et al., "Indocyanine green: observations on its physical properties, plasma decay, and hepatic extraction," *J. Clin. Invest.* **39**(1), 592–600 (1960).
37. N. Fogh-Andersen, B. Altura, and B. Altura, "Composition of interstitial fluid," *Clin. Chem.* **41**(10), 1522–1525 (1995).
38. N. E. Miller et al., "Secretion of adipokines by human adipose tissue in vivo: partitioning between capillary and lymphatic transport," *Am. J. Physiol. Endocrinol. Metab.* **301**(4), E659–E667 (2011).
39. S. G. Rockson, "Lymphedema," *Am. J. Med.* **110**(4), 288–295 (2001).
40. P. Tso, V. Pitts, and D. Granger, "Role of lymph flow in intestinal chylomicron transport," *Am. J. Physiol.* **249**(1), G21–G28 (1985).
41. Y. Ashitate et al., "Near-infrared fluorescence imaging of thoracic duct anatomy and function in open surgery and video-assisted thoracic surgery," *J. Thorac. Cardiovasc. Surg.* **142**(1), 31–38 (2011).
42. Y. Takema et al., "Age-related changes in the elastic properties and thickness of human facial skin," *Br. J. Dermatol.* **131**(5), 641–648 (1994).
43. M. J. McShane et al., "Monte Carlo modeling for implantable fluorescent analyte sensors," *IEEE Trans. Biomed. Eng.* **47**(5), 624–632 (2000).
44. A. A. Gashev et al., "Regional variations of contractile activity in isolated rat lymphatics," *Microcirculation* **11**(6), 477–492 (2004).
45. J. Benoit et al., "Characterization of intact mesenteric lymphatic pump and its responsiveness to acute edemagenic stress," *Am. J. Physiol.* **257**(6), H2059–H2069 (1989).